Atomic Spectroscopy

Article

Laser-Induced Breakdown Spectroscopy (LIBS) for the Characterization of Methane-Air Laminar Diffusion Flame

Gangfu Rao,[a,b] Meirong Dong, [a,b,*] Wei Nie, [a,b] Xiao Lin, [a,b] Youcai Liang,[a,b] and Jidong Lu [a,b]

[a] School of Electric Power, South China University of Technology, Guangzhou, Guangdong, 510640, P. R. China

[b] Guangdong Province Engineering Research Center of High Efficient and Low Pollution Energy Conversion, Guangzhou, Guangdong, 510640, P.R. China

Received: *April 23, 2021;* ***Revised:*** *May 18, 2021;* ***Accepted:*** *May 18, 2021;* ***Available online:*** *May 19, 2021.*

DOI: 10.46770/AS.2021.099

ABSTRACT: Laser-induced breakdown spectroscopy (LIBS) was applied for the characterization of the methane-air laminar diffusion flame, revealing the spatial distribution of its composition. From the measurement, it was found that distribution of the atomic and ionic N emissions produced by the flame had obvious differences, which were mainly distributed in the air area and flame area, respectively. A comparison of the LIBS spectra of air, methane gas, and methane-air laminar diffusion flame showed that the atomic N emissions were mainly produced by the excitation of N_2, and the ionic N emissions were more related to the N-containing combustion products. In addition, the correlation between typical emissions and the flame temperature measured by thermocouple was estimated to show that the tendency of the changes in temperature can be characterized by C_2 emission intensities. This work provides a new method for real-time online flame temperature measurement, and also provides a reference for revealing the formation process and conversion pathway of each component in the flame.

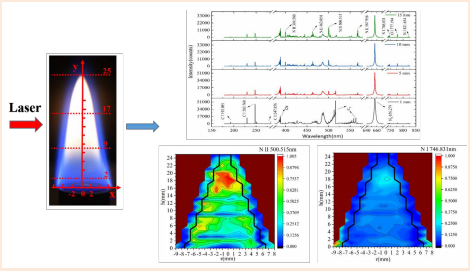

INTRODUCTION

Fuel combustion is a common phenomenon in nature and involves a complex physical and chemical process. The energy and heat transfer in this process couples the interaction between the flow and the chemical reactions. As a common fuel, methane (CH_4) is the most abundant hydrocarbon on earth widely used in industrial production and in daily life. Therefore, it is important to deeply understand the dynamic characteristics of methane combustion for improving its utilization efficiency.

Over the past decades, research has aimed to understand the combustion characteristics of CH_4. Hou *et al.*[1] proposed a set of reduced mechanisms for sensitivity analysis of CH_4-O_2 combustion in a liquid rocket engine. Zhang *et al.*[2] studied the effect of initial temperature on the minimum ignition energy and combustion characteristics of a CH_4-air mixture. Yan *et al.*[3] investigated the catalytic combustion of premixed CH_4-air in the meso-combustor with and without preheating channels at steady conditions by the numerical method. Cui *et al.*[4] used a hedging flame model with CHEMKIN software to analyze the influence of water vapor on methane hydrate combustion. In addition, they also analyzed the influence of the diameter of the methane hydrate sphere and the initial center core temperature during the combustion process.[5] All of these traditional analysis methods can be used to understand the combustion mechanism to a certain extent, but the detailed kinetic parameters cannot be obtained based on in-situ and intermediate product components during the combustion process.

With the development of optical technologies, several non-intrusive methods were applied for combustion diagnosis, including the spontaneous emission spectrum and laser diagnostic methods. Sun *et al.*[6] measured the temperature and emissivity of the gasoline flame and the coal-fired flame according to the gray property of flames based on spectral analysis and the two-color method. Krabicka *et al.*[7] combined the electron-multiplying charge-coupled device (EMCCD) to monitor the specific flame radicals (OH, CN, CH, and C_2), and established the correlation between radical characteristics and air-to-fuel ratios of the premixed C_3H_8-air flame. Lou *et al.*[8] reconstructed the distribution

of the temperature and the soot volume fraction from monochromatic radiative intensity images with the visible spectrum range in a laminar ethylene diffusion flame. However, the measurement of spontaneous emission spectra is limited by the intensity of flame radiation.

Laser diagnostics technology uses laser light to obtain relevant spectral information, which helps to improve the intensity of the detection signal and the signal-to-noise ratio. Wang *et al.*[9] presented an innovative tomographic method using tunable diode laser absorption spectroscopy (TDLAS) and the algebraic reconstruction technique (ART) to detect the temperature and H_2O concentration in flat CH_4-air premixed flames under three different equivalence ratios. Li *et al.*[10] proposed the 3D flame structure diagnostics based on tomographic laser-induced fluorescence (Tomo-LIF) of OH radicals, which was successfully applied in a CH_4-air premixed laminar flame and a non-premixed turbulent CH_4 jet flame. Pillier *et al.*[11] analyzed the influence of the C_2 and C_3 compounds in natural gas on the generation of NO in the flame based on LIF and cavity ring-down spectroscopy (CRDS). Thus, the multi-components and temperature measured by these approaches need the lasers under different wavelengths in conjunction with a complicated instrumental system.

Laser-induced breakdown spectroscopy (LIBS) is a newly emerging optical detection method with the advantages of rapid, simultaneous monitoring of multi-elements, high temporal and spatial resolution, *etc.*, and has been applied in a wide variety of fields, such as biomedicine,[12-15] cultural heritage and archaeology,[16-18] metallurgical analysis,[19-21] agricultural materials,[22-25] and so on. Recently, it has also been used for combustion diagnosis, including solid fuel combustion[26-28] and gas fuel combustion.[29-31] Do *et al.*[32] selected atomic emission line intensity based on LIBS to establish the correlation between the line intensity and the hydrocarbon fuel concentration. Wu *et al.*[31] established a correlation between the line intensities and the local fuel-air ratio in both laminar and turbulent CH_4-air flames. Kiefer *et al.*[33] realized the local temperature and the equivalence ratio measurement in CH_4-air and dimethyl ether (DME)-air flames by using LIBS. Kotzagianni *et al.*[29] used LIBS to determine local structures of premixed laminar hydrocarbon-air flames through laser breakdown threshold. Majd *et al.*[34] used spatially resolved laser-induced breakdown spectroscopy (SR-LIBS) to quantitatively estimate the local equivalence ratio of CH_4-air diffusion flames. They also determined the width of the secondary combustion region at a specified height above the burner in CH_4-air diffusion flames according to the threshold energy. In our previous work, we conducted the spatially resolved LIBS in laminar premixed CH_4-air flames to characterize the flame structure and proposed a method for the width and distribution of different flame regions based on the plasma energy coupled with LIBS spectra.[35] However, there was little in-depth correlation analysis between the elemental characteristics and the intermediate and final combustion products, which is of great significance to clarify the distribution and conversion path of each component in order to further reveal the combustion mechanism.

In this work, the combustion characteristics of the CH_4-air laminar diffusion flame, which is a basic flame model, were investigated based on LIBS. The correlation between the characteristic spectra and the combustion components was investigated to reveal the spatial distribution of the components during the combustion process, which provides an experimental basis for studying the generation and transformation of the combustion composition. In addition, the relationship between the spectral characteristics and the flame temperature was further analyzed to realize the real-time detection of the flame temperature.

EXPERIMENTAL

Experimental. The instrumental system used for this study was set up as shown in Fig. 1(a), which can be divided into two parts. The first part was the LIBS system that utilized the Nd:YAG laser (Continuum, Surelite) as the source to generate a high-energy pulse beam (wavelength 1064 nm, pulse duration 6 ns, diameter 7 mm). The laser energy was set to 410 mJ and the laser frequency was set to 1 Hz. The pulse beam was focused by a focusing lens (f = 200 mm) on the flame central axis plane to create a plasma, which was then collected by a 100 mm focal lens and transmitted to a four-channel spectrometer (Avantes, wavelength 180 to 815 nm, resolution 0.10 to 0.22 nm) through the optical fibers. The digital delay controller (DG535, Stanford Research System) was used to control the laser and spectrometer synchronously. The optimal delay time between the acquisition signal time of the spectrometer and the working time of the laser was selected in order to obtain the atomic and ionic spectral lines with a high signal-to-noise ratio as the standard. After optimization, 1280 ns (minimum delay time of the spectrometer) was selected as the delay time. At the same time, in order to obtain a higher time resolution, the minimum integration time (1.05 ms) of the spectrometer was selected as the integration time.

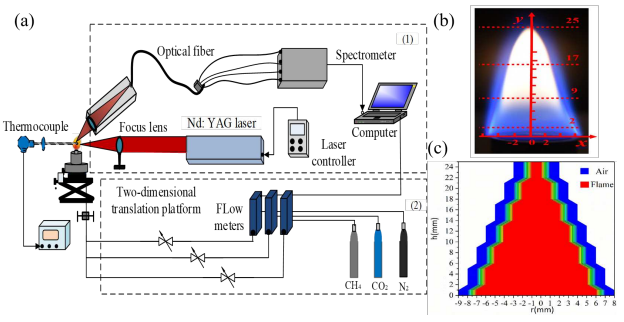

Fig. 1 Schematic diagram of the experimental setup: (a) LIBS for combustion system, (b) the measured flame picture, (c) the measurement coordinate system of flame area and air area.

Fig. 2 LIBS spectra of flame at different axial heights: (a) 180 to 815 nm, (b) ionic N lines.

The second part of the measurement system was the combustion system. A co-flow laminar diffusion flame burner was used to generate an axisymmetric laminar diffusion flame with CH_4. The CH_4 gas entered the burner from four intake pipes, then ejected from the nozzle and diffused freely into the ambient atmosphere to realize the diffuse combustion by the artificial ignition method. The inner diameter of the nozzle was approximately 10 mm. The mass flow meter (CS200, Sevenstar) was used to control the gas flow rate. The flow rate of CH_4 was set at 150 mL/min to obtain a relatively stable laminar flame and the flame picture is shown in Fig. 1(b).

The burner was placed on a three-dimensional translation stage, and the laser pulse was focused on different positions of the flame by adjusting the translation stage. In order to facilitate the description of the measuring points, a rectangular coordinate system was established with the center of the nozzle as the origin of the coordinates, as shown in Fig. 1(c), including the coordinates of the flame area and the air area. The measuring points were the space area within the range of 0 to 25 mm for the axial coordinate and -9 to 8 mm for the radial coordinate. The spectrum was collected once per pulse and 100 spectra were collected at each point, then the average value of 100 spectra was taken as the analytical data. The spacing between each spatial point was approximately 1 mm. In order to thoroughly understand the spectra characteristics with the flame temperature, the thermocouple (S type, wires diameter 0.5 mm, temperature range 0 to 1600 ℃) was coupled to measure the temperature of each measuring point, where the probe was placed perpendicular to the central axis of the flame. It was basically consistent with the position of the focal point of the laser at each measuring point.

Analytical methods. The gradient of change can reflect the spatial amount consumed or generated by the target object and its rate of chemical reactions. Therefore, the gradient of the N and O emissions on the spatial scale were also analyzed. It can be seen from Fig. 1(b) that the flame presents an axisymmetric structure. The calculation formula for the gradient on the left side of the central axis is described in Equation (1).

$$x_{cr1} = (x_{m-1,n} - x_{m,n}) \div s \qquad \text{(Eq. 1)}$$

where x_{cr1} represents the gradient of coordinates (m, n), $x_{m-1,n}$ represents the spectral intensity of the coordinate (m-1, n), $x_{m,n}$ represents the spectral intensity of the coordinate (m, n), where the range of m is -8 to 0, and the range of n is 0 to 25. s represents the space distance of the two coordinate points, which is 1 mm.

Similarly, the gradient on the right side of the central axis is described in Equation (2).

$$x_{cr2} = (x_{m+1,n} - x_{m,n}) \div s \qquad \text{(Eq. 2)}$$

where x_{cr2} represents the gradient of coordinates (m, n), $x_{m+1,n}$ represents the spectral intensity of the coordinate (m+1, n), $x_{m,n}$ represents the spectral intensity of the coordinate (m, n), where the range of m is 1 to 7 and the range of n is 0 to 25.

In this work, the spectral data collected were processed by baseline correction (asymmetric least squares baseline correction algorithm). The (0, 1) normalization method was also applied to process the spatial intensity distribution of the spectral lines. The ratio of the spectral line intensity value of each measuring point to the maximum value of the spectral line intensity in the entire measuring area was used instead of the spectral line intensity value of the measuring point.

RESULTS AND DISCUSSION

LIBS emissions produced from the flame. Fig. 2(a) shows the typical emission spectra of laser-induced plasma produced from the CH_4-air diffusion flame corresponding to the range of 180 to 815 nm for different spark locations above the burner rim in the combustion center line (1 mm, 5 mm, 10 mm, and 15 mm). The measured wavelength and reference wavelength of the characteristic spectra in the experiment are summarized in Table 1,

Table 1. Comparison of Reference and Measured Wavelength of Characteristic Spectra[36-37]

Spectral type	Reference wavelength			Measured wavelength		
C I	193.091	247.856	283.760	193.097	247.870	283.715
CN	388.29	/	/	388.477	/	/
	399.500	410.995	415.148	399.532	410.854	415.207
N II	463.054	444.703	493.512	462.971	444.650	493.483
	500.515	567.956	594.465	500.239	567.874	594.052
C_2	516.42	/	/	516.423	/	/
N I	746.831	821.634	/	746.822	821.636	/
O I	422.276	532.910	777.194	422.330	532.928	777.033
H_α	656.279	/	/	656.126	/	/

Fig. 3 Spatial distribution of (a) N I 746.831 nm and (b) O I 777.194 nm emissions. Notes: The black line in the figure is the boundary between the air area and the flame area.

where the reference wavelength of the atomic and molecular lines can be obtained from the NIST Atomic Spectra Database[36] and in Ref.[37], respectively.

It was found that the dominant emission spectra were changed as the axial height increased. The emission lines of H_α 656.279 nm, O I 777.194 nm, C I 247.856 nm, CN 388.29 nm, and C_2 516.42 nm appeared clearly at the nozzle. As the axial height increased, the spectral intensity of CN, C_2 and C began to gradually weaken; the atomic emissions of N and O began to gradually increase; and the spectral intensity of H also became weak to a certain extent. Fuel-rich combustion occurs near the nozzle, where the fuel is excessive. Along the axial direction, it gradually turns into stoichiometric combustion and fuel-lean combustion, causing the fuel gradually to decrease and the air increase by degrees. Apart from this, with the increase of axial height, the ionic N lines such as N II 399.500 nm, N II 463.054 nm, N II 500.515 nm, N II 567.956 nm began to appear and gradually became significant, as shown in Fig. 2(b).

Spatial distribution of N and O emissions from the flame. To characterize the diffusion effect of nitrogen and oxygen in the air and the chemical reaction with oxygen, the spatial distribution of the normalized N and O emissions produced from the flame central axis plane were obtained, as shown in Fig. 3. It can be seen that the atomic nitrogen (N I 746.831 nm) and oxygen (O I 777.194 nm) had a similar spatial distribution on the central axis plane. Both of them had the strongest zone in the air area and the sub-strong zone above 18 mm from the nozzle along the central axis.

The calculated spatial gradient was normalized and is presented in Fig. 4. It can be seen that both the nitrogen and oxygen had a large positive gradient in the air area and a negative gradient in the

Fig. 4 Spatial distribution of spatial gradient for (a) N I 746.831 nm and (b) O I 777.194 nm. Notes: The black line in the figure is the boundary between the air area and the flame area.

Fig. 5 Spatial distribution of ionic N emissions: (a) N II 399.500, (b) N II 463.054, (c) N II 500.515, (d) N II 567.956 and atomic N emissions: (e) N I 746.831, (f) N I 821.634. Notes: The black line in the figure is the boundary between the air area and the flame area.

flame edge area. The main reason is that the air was continuously diluted and consumed due to the diffusion and chemical reaction, so that the gradient appeared positive in the air area. As shown in Fig. 8, the temperature difference is large in the flame edge area, and the temperature of the flame edge area is higher than the temperature of other areas. The high temperature would speed up the reaction rates, resulting in a negative gradient at the edge of the methane diffusion flame.

As shown in Fig. 2(b), when the distance from the nozzle increased, the ionic N lines began to appear and gradually became significant. The normalized intensity spatial distribution of atomic N (N I 746.831 nm and N I 821.634 nm) and ionic N (N II 399.500 nm, N II 463.054 nm, N II 500.515 nm, N II 567.956 nm) on the flame central axis plane was obtained, as shown in Fig. 5. It was also seen that the atomic N and ionic N lines had different spatial distributions. The ionic emissions (N II 399.500 nm, N II 463.054 nm) were distributed in most of the flame area; the ionic emissions (N II 500.515 nm, N II 567.956 nm) were mainly distributed in the flame edge area. All of the strongest zones of the ionic emissions were dominated in the area above the nozzle at 18 mm along the central axis. While for the atomic emissions (N I 746.831 nm and N I 821.634 nm), the strongest zone appeared in the air, and the sub-strong zone also appeared in the area above the nozzle at 18 mm along the axial direction, which is similar to the distribution of O I 777.194 nm.

To further explore the reasons for the origin of the characteristic spectral emissions from nitrogen and its correlation with the combustion components, the LIBS spectra of air, CH_4 gas, and CH_4-air diffusion flame after normalization and baseline correction were analyzed comparatively, as shown in Fig. 6(a).

Fig. 6 Comparison of LIBS spectra with different atmosphere and temperature: (a) air (20℃), CH_4 gas, CH_4-air diffusion flame; (b) air (20℃), air (120℃), air (260℃), air (330℃), air (400℃).

Fig. 7 Spatial distribution of CH_4 related emissions produced from the flame: (a) C I 247.856 nm, (b) CN 388.29 nm, (c) C_2 516.42 nm, (d) H_α 656.279 nm. Notes: The black line in the figure is the boundary between the air area and the flame area.

The flow rates of CH_4 either for the pure CH_4 gas or the combustion were kept the same at 150 mL/min. The air spectrum was obtained directly from the atmospheric environment with laser. In order to minimize the interference of the diffusion effect, the measurement position of air and CH_4 gas were all set at 2 mm above the nozzle along the central axis of the burner of the centerline, and the CH_4-air diffusion flame was at 15 mm above the nozzle of the burner along the central axis.

By comparing the LIBS spectra (see Fig. 6), it was seen that the atomic characteristic emissions such as N I 746.831 nm and N I 493.512 nm can be observed from the ablation of air due to the presence of N_2 in the air, but ionic N emissions were weak. On the contrary, obvious ionic N emissions can be observed in the flame, while the atomic emissions were relatively weak.

The temperature can increase the energy of the electrons, which may make them transition to higher energy levels and produce nitrogen ionic lines. In Fig. 6(b), the nitrogen spectral lines are shown after baseline correction and normalization of the air at different temperatures. In Fig. 6(b), it can be seen that the temperature had little effect on the nitrogen spectra in the air. At different temperatures, only the nitrogen atomic lines can be found and no obvious nitrogen ionic lines were observed. Therefore, the temperature was not the main reason that affects the appearance of the nitrogen ionic lines; the nitrogen ionic lines were mainly generated by the excitation of the combustion products.

It is well known that nitrogen oxides (NOx) are produced in the presence of nitrogen in the air during CH_4-air diffusion combustion. According to the different oxidation mechanisms and sources of the N atom, NO_X is generally formed via prompt, thermal, N_2O, and the fuel pathways,[38] while for CH_4 combustion, NO_X would not be produced through the fuel pathway. Monaghan *et al.*[38] indicated that for the CH_4-air diffusion round-jet flame, for total NOx, 47% was due to the prompt pathway, 32% was due to the N_2O pathway, and 21% was due to the thermal pathway. As shown in Fig. 5, N II 500.515 nm and N II 567.956 nm were mainly distributed in the flame edge area, which was similar to the spatial distribution of NO in the diffusion flame as shown by Sullivan *et al*.[39] and Monaghan *et al.*[38] While the temperature accelerated the NO_X reaction rate,[40] it also reduced the spectral intensity.[33] Compared with the suppression effect of the temperature on spectral intensity, which can be seen from Fig. 5 in the flame edge area, the promotion effect of the temperature on the chemical reaction of NO production was dominant. Therefore, N II 500.515 nm and N II 567.956 nm may be produced by excitation of NOx, such as NO. Besides, N II 399.500 nm and N II 463.054 nm may be mainly produced by the excitation of N-containing combustion intermediate products.

in Fig. 7. It was seen that different atomic or molecular spectral emissions had different spatial distribution characteristics in the flame. The strongest zone of C I 247.856 nm, CN 388.29 nm, C_2 516.42 nm, H_α 656.279 nm appeared near the nozzle due to the presence of the main component, CH_4.

It is worth noting that C I 247.856 nm had two sub-strong zones above the nozzle at 14 mm and 17 mm along the central axis, which may be due to the fact that the amount of O_2 in the inner region of the flame was small, an oxygen-lean combustion, so that the product was a C-containing product, such as CO. As the axial height increased, the diffusion effect of O_2 began to be significant, and CO was further oxidized to produce C-containing products, such as CO_2. Jin *et al*.[41] and Lim *et al*.[42] used numerical simulation and also found that in the CH_4 co-flow diffusion flame and counterflow diffusion flames, compared with CO_2, the spatial location of the maximum mole fraction of CO was closer to the nozzle, respectively.

Fig. 8 Spatial distribution of CH_4-air diffusion flame temperature measured by thermocouple. Notes: The black line in the figure is the boundary between the air area and the flame area.

Temperature measurement of flame based on C_2 emissions. Temperature is one of the most important parameters in combustion diagnosis, which has significant reference value for studying fuel combustion performance. The temperature of each measuring point measured by thermocouple is shown in Fig. 8. It can be seen that the lowest flame temperature zone is near the nozzle. In the axial direction, the temperature is raised as the axial height increased; in the radial direction, the temperature is raised as the radius increased.

The typical LIBS emission lines at each height were chosen to analyze the correlation with the temperature on the central axis. Different spectral line intensities and temperature values were quite different. In order to make it easier to compare their changing trends with the increase in axial height, different spectral line intensities and temperatures were reduced by different multiples. The results in Fig. 9 show that the peak intensity of C I 247.856 nm and C_2 516.42 nm indicates a rapid decrease first, then a slow decrease trend with the increase of the axial height. On the contrary, with the increase of the axial height, the temperature showed a rapid increase first and then a gradually increasing trend. In order to estimate the correlation between the head peak intensity and the temperature, the C I 247.856 nm and C_2 516.42 nm head peak intensity at the central axis of the CH_4-air diffusion flame was fitted with the temperature to obtain the calibration model. The results are presented in Fig. 10.

Fig. 9 Comparison of LIBS characteristic spectra and temperature of flame axis. Notes: The error bar of the spectra was the standard error of 100 spectra, and the error bar of the temperature was the standard error of eight measurements.

Spatial distribution of C, H, CN and C_2 emissions from the flame. The spatial distribution of representative atomic and molecular characteristic emissions of C I 247.856 nm, CN 388.29 nm, C_2 516.42 nm, H_α 656.279 nm was also analyzed, as shown

On the central axis, the fitting function of the C_2 head peak intensity and temperature is shown in Equation (3), the R^2 was 0.962. The fitting function of the C peak intensity and temperature is shown in Equation (4), the R^2 was 0.908.

$$y = 954 - 0.00685x + 268 \times 0.99894^x \quad \text{(Eq. 3)}$$

where x represents C_2 516.42 nm head peak intensity, y represents the reference temperature measured by the thermocouple.

Fig. 10 The head peak intensity and temperature fitting diagram at the central axis of the flame: (a) C_2 516.42 nm, (b) C I 247.856 nm. Notes: The error bar of the spectra was the standard error of 100 spectra, and the error bar of temperature was the standard error of eight measurements.

$$y = -1478 + 0.02748x + 2796 \times 0.99997^{x} \quad \text{(Eq. 4)}$$

where x represents C I 247.856 nm peak intensity, y represents the reference temperature measured by the thermocouple.

Compared with C I 247.856 nm, the fitting function of C_2 516.42 nm peak intensity and temperature obtains a higher R^2, so Equation (3) was used to predict the temperature of all measuring points, and then compared with the temperature measured by the thermocouple to test the reliability of the model. Relative Error (*RE*) was used as an evaluation index and the calculation formula is shown in Equation (5).

$$RE = \left| \frac{x - u}{u} \right| \times 100\% \quad \text{(Eq. 5)}$$

where x represents the temperature calculated by the function model, u represents the reference temperature measured by the thermocouple.

The spatial distribution of *RE* from each measuring point is shown in Fig. 11, including the *RE* values of all spatial measuring points (Fig. 11(a)), and the spatial distribution of the details of *RE* less than 10% (Fig. 11(b)). It can be seen that, except for the high *RE* at the nozzle and the air, the *RE* value of most areas of the flame was within 10%, indicating that it was feasible to calculate the flame temperature with C_2 516.42 nm. The reason for the high *RE* near the nozzle may be that the flow velocity at this area was high, which affects the measurement accuracy of the thermocouple. In the area close to the air, the C_2 516.42 nm spectra was really weak or even undetectable, which caused the *RE* value of the air to be relatively high.

Fig. 11 Spatial distribution of *RE* from the calculated temperature and the temperature measured by the thermocouple: (a) *RE* values of all spatial measurement points, (b) details of *RE* value less than 10%. Notes: The black line in the figure is the boundary between the air area and the flame area.

CONCLUSIONS

Laser-induced breakdown spectroscopy has been applied for the measurement of methane-air laminar diffusion flame to obtain the spatial atomic, ionic and combustion species. It was found that the N atomic lines of N I 746.831 nm and N I 821.634 nm were mainly produced by the excitation of N_2 in the air; the ionic N lines of N II 399.500 nm, N II 463.054 nm, N II 500.515 nm, and N II 567.956 nm were distributed in the flame area and mainly generated by excitation of N-containing combustion products. In addition, the correlation between the typical spectral characteristics and flame temperature measured by thermocouple

was analyzed and a good correlation was found between the C_2 emission and the flame temperature, which indicated that LIBS can reflect the information of the temperature. All of the measurement results obtained indicate the reference information necessary for understanding the formation and transformation of the various components in the combustion process, and provides a new method for flame temperature measurements.

AUTHOR INFORMATION

Corresponding Author

* M. R. Dong

Email address: epdongmr@scut.edu.cn

Notes

The authors declare no competing financial interest.

ACKNOWLEDGMENTS

The research was supported by the National Natural Science Foundation of China (51976064) and the Guangdong Basic and Applied Basic Research Foundation (2020A1515010646). We also acknowledge the support from the Guangdong Province Key Laboratory of Efficient and Clean Energy Utilization (2013A061401005) and the Key Laboratory of Efficient and Clean Energy Utilization of Guangdong Higher Education Institutes (KLB10004).

REFERENCES

1. J. L. Hou, P Jin, and G. B Cai, *J. Aerosp. Power*, 2012, **27,** 1549-1554. https://doi.org/10.13224/j.cnki.jasp.2012.07.029
2. Q. Zhang and W. Li, *Process Saf. Prog.*, 2013, **32,** 37-41. https://doi.org/10.1002/prs.11561
3. Y. F. Yan, S. Feng, Z. Z. Huang, L. Zhang, W. L. Pan, L. X. Li, and Z. Q. Yang, *Int. J. Energy Re.*, 2018, **42,** 999-1012. https://doi.org/10.1002/er.3887
4. G. Cui, Z. R. Dong, S. Wang, X. Xing, T. X. Shan, and Z. L. Li, *Appl. Energy*, 2020, **259,** 114205. https://doi.org/10.1016/j.apenergy.2019.114205
5. G. Cui, S. Wang, Z. R. Dong, X. Xing, T. X. Shan, and Z. L. Li, *Appl. Energy*, 2020, **257,** 114058. https://doi.org/10.1016/j.apenergy.2019.114058
6. Y. P. Sun, C. Lou, and H. C. Zhou, *Proc. Combust. Inst.*, 2011, **33,** 735-741. https://doi.org/10.1016/j.proci.2010.07.042
7. J. Krabicka, G. Lu, and Y. Yan, *IEEE Trans. Instrum. Meas.*, 2011, **60,** 1854-1860. https://doi.org/10.1109/TIM.2010.2102411
8. C. Lou and H. C. Zhou, *Numerical Heat Transfer, Part A*, 2009, **56,** 153-169. https://doi.org/10.1080/10407780903107246
9. F. Wang, Q. Wu, Q. X. Huang, H. D. Zhang, J. H. Yan, and K. Cen, *Opt. Commun.*, 2015, **346,** 53-63. https://doi.org/10.1016/j.optcom.2015.02.015
10. T. Li, J. Pareja, F. Fuest, M. Schütte, Y. H. Zhou, A. Dreizler, and B. Böhm, *Meas. Sci. Technol.*, 2018, **29,** 015206. https://doi.org/10.1088/1361-6501/aa938a
11. L. Pillier, A. El Bakali, X. Mercier, A. Rida, J. F. Pauwels, and P. Desgroux, *Proc. Combust. Inst.*, 2005, **30,** 1183-1191. https://doi.org/10.1016/j.proci.2004.08.057
12. A. El-Hussein, A. K. Kassem, H. Ismail, and M. A. Harith, *Talanta*, 2010, **82,** 495-501. https://doi.org/10.1016/j.talanta.2010.04.064
13. L. Sancey, V. Motto-Ros, S. Kotb, X. C. Wang, F. Lux, G. Panczer, J. Yu, and O. Tillement, *J. Vis. Exp.*, 2014, **88,** e51353. https://doi.org/10.3791/51353
14. Y. Markushin, N. Melikechi, A. Marcano O, S. Rock, E. Henderson, and D. Connolly, *Proc. of SPIE*, 2009, **7190**, 719015. https://doi.org/10.1117/12.810247
15. X. Y. Liu and W. J. Zhang, *J. Biomed. Sci. Eng.*, 2008, **1,** 147-151. https://doi.org/10.4236/jbise.2008.13024
16. A. Botto, B. Campanella, S. Legnaioli, M. Lezzerini, G. Lorenzetti, S. Pagnotta, F. Poggialini, and V. Palleschi, *J. Anal. At. Spectrom.*, 2019, **34,** 81-103. https://doi.org/10.1039/c8ja00319j
17. M. A. Kasem, J. J. Gonzalez, R. E. Russo, and M. A. Harith, *Spectrochim. Acta, Part B*, 2014, **101,** 26-31. http://dx.doi.org/10.1016/j.sab.2014.07.010
18. A. Giakoumaki, K. Melessanaki, and D. Anglos, *Anal. Bioanal. Chem.*, 2007, **387,** 749-760. https://doi.org/10.1007/s00216-006-0908-1
19. L. F. Qi, L. X. Sun, Y. Xin, Z. B. Cong, Y. Li, and H. B. Yu, *Plasma Sci. Technol.*, 2015, **17,** 676-681. https://doi.org/10.1088/1009-0630/17/8/11
20. Q. Zeng, C. Y. Pan, T. Fei, X. K. Ding, S. B. Wang, and Q. P. Wang, *J. Appl. Spectrosc.*, 2018, **85,** 817-822. https://doi.org/10.1007/s10812-018-0723-4
21. F. Z. Dong, X. L. Chen, Q. Wang, L. X. Sun, H. B. Yu, Y. X. Liang, J. G. Wang, Z. B. Ni, Z. H. Du, Y. W. Ma, and J. D. Lu, *Front. Phys.*, 2012, **7**, 679-689. https://doi.org/10.1007/s11467-012-0263-y
22. M. Y. Yao, L. Huang, J. H. Zheng, S. Q. Fan, and M. H. Liu, *Opt. Laser Technol.*, 2013, **52,** 70-74. http://dx.doi.org/10.1016/j.optlastec.2013.04.005
23. N. Sharma, Y. Khajuria, V. K. Singh, S. Kumar, Y. Lee, P. K. Rai, and V. K. Singha, *At. Spectrosc.*, 2020, **41**(3), 110-118. https://doi.org/10.46770/AS.2020.03.003
24. N. Sharma, V. K. Singh, Y. Lee, S. Kumar, P. K. Rai, A. K. Pathak, and V. K. Singha, *At. Spectrosc.*, 2020, **41**(6), 234-241. https://doi.org/10.46770/AS.2020.06.003
25. W. A. Farooq, K. G. Rasool, W. Tawfik, and A. S. Aldawood, *Plasma Sci. Technol.*, 2015, **17,** 948-952. https://doi.org/10.1088/1009-0630/17/11/11
26. Y. Z. Liu, K. D. Wan, Y. He, Z. H. Wang, J. Xia, and K. Cen, *Fuel*, 2020, **260,** 116346. https://doi.org/10.1016/j.fuel.2019.116346
27. Y. Z. Liu, Z. H. Wang, J. Xia, L. Vervisch, K. D. Wan, Y. He, R. Whiddon, H. Bahai, and K. Cen, *Proc. Combust. Inst.*, 2019, **37,** 2681-2688. https://doi.org/10.1016/j.proci.2018.06.042
28. Y. Yuan, S. Q. Li, and Q. Yao, *Proc. Combust. Inst.*, 2015, **35,** 2339-2346. http://dx.doi.org/10.1016/j.proci.2014.07.016
29. M. Kotzagianni, E. Kakkava, and S. Couris, *Appl. Spectrosc.*, 2016, **70,** 627-634. https://doi.org/10.1177/0003702816631296

30. L. Merotto, M. Sirignano, M. Commodo, A. D'Anna, R. Dondè, and S. D. Iuliis, *Energy Fuel.*, 2017, **31,** 3227-3233. https://doi.org/10.1021/acs.energyfuels.6b03094
31. Y. Wu, M. Gragston, Z. L. Zhang, P. S. Hsu, N. Jiang, A. K. Patnaik, S. Roy, and J. R. Gord, *Combust. Flame*, 2018, **198,** 120-129. https://doi.org/10.1016/j.combustflame.2018.09.009
32. H. Do and C. Carter, *Combust. Flame*, 2013, **160,** 601-609. http://dx.doi.org/10.1016/j.combustflame.2012.12.002
33. J. Kiefer, J. W. Tröger, Z. S. Li, and M. Aldén, *Appl. Phys. B*, 2011, **103,** 229-236. https://doi.org/10.1007/s00340-010-4338-6
34. A. E. Majd, A. S. Arabanian, R. Massudi, and M. Nazeri, *Appl. Spectrosc*., 2011, **65,** 36-42. https://doi.org/10.1366/10-05863
35. Z. H Tian, M. R. Dong, S. S. Li, and J. D. Lu, *Spectrochim. Acta, Part B*, 2017, **136,** 8-15. https://doi.org/10.1016/j.sab.2017.08.001
36. https://physics.nist.gov/PhysRefData/ASD/lines_form.html
37. S. J. Mousavi, M. H. Farsani, S. M. R. Darbani, A. Mousaviazar, M. Soltanolkotabi, and A. Eslami Majd, *Appl. Phys. B.*, 2016, **122,** 106. https://doi.org/10.1007/s00340-016-6371-6
38. R. F. D. Monaghan, R. Tahir, A. Cuoci, G. Bourque, M. Füri, R. L. Gordon, T. Faravelli, A. Frassoldati, and H. J. Curran, *Energy Fuel.*, 2012, **26,** 1598-1611. https://doi.org/10.1021/ef201853k
39. N. Sullivan, A. Jensen, P. Glarborg, M. S. Day, J. F. Grcar, J. B. Bell, and C. J. Pope, *Combust. Flame*, 2002, **131,** 285-298. https://doi.org/10.1016/S0010-2180(02)00413-3
40. A. A. Z. Ahmed, H. O. H. Kayed, M. M. A. Hassan, and E. E. Khalil. *51st AIAA/SAE/ASEE Joint Propulsion Conf. (Orlando, FL, USA)*, 2015. https://doi.org/10.2514/6.2015-4093
41. H. F Jin, A. Frassoldati, Y. Z. Wang, X. Y. Zhang, M. R. Zeng, Y. Y. Li, F. Qi, A. Cuoci, and T. Faravelli, *Combust. Flame*, 2015, **162,** 1692-1711. https://doi.org/10.1016/j.combustflame.2014.11.031
42. J. Lim, J. Gore, and R. Viskanta, *Combust. Flame*, 2000, **121,** 262-274. https://doi.org/10.1016/S0010-2180(99)00137-6